Journal of Materials Chemistry A

Accepted Manuscript

ROYAL SOCIETY OF CHEMISTRY

www.rsc.org/materialsA

Interfacial Nitrogen Stabilizes Carbon-Coated Mesoporous Silicon Particle Anodes

Xiang Han,[†] Huixin Chen,[‡] Xin Li[†], Jianyuan Wang[†], Cheng Li,[†] Songyan Chen,[*†] and Yong Yang[*‡]

[†]*Semiconductor Photonics Research Center, Department of Physics, Xiamen University, Xiamen361005, P. R. China*
E-mail: sychen@xmu.edu.cn
[‡]*State Key Laboratory for Physical Chemistry of Solid Surfaces, Department of Chemistry, Xiamen University, Xiamen361005, P. R. China*
E-mail: yyang@xmu.edu.cn

Abstract

We report for the first time that the dehydrogernation process of PAN was depressed and the surface silicon oxide outer MSP was reduced during annealing in Ar+H_2. Consequently, the remaining -NH bands of the carbon chain can interact with the surface fresh amorphous Si to form Si-N-C layer, which improves the adhesion between Si and C and serves as a stable electrolyte blocking layer. In addition, based on micron-sized MSP, the structural stability of the electrode is dramatically enhanced through in-situ forming Si nanocrystals at downsizing 5nm. The low Li^+ diffusion kinetics of Si-N-C layer and self limiting inhomogeneous lithiation in MSP jointly creates unlithiated Si nanocrystals, acting as supporting frame to prevent pulverization of the anode material. Our nitrogen engineering MSP anode has marked for the first time that a 100% capacity retention (394 mA h g^{-1}) after 2000 cycle (10 cycles each at 0.1, 0.5, 1, 2, and 1 and then 1950 cycles at 0.5 A g^{-1}) and a 100% capacity retention at 0.1 A g^{-1} (540 mA h g^{-1}) after 400 cycles. Thus, our work proposes a novel avenue to engineer battery materials with large volume changes.

1 Intoduction

Unstable solid-electrolyte interphase (SEI) and particle fracture have been regarded as primary reasons for the capacity attenuation of silicon-based anodes [1-4]. Pioneering researches have shown that downsizing to the nanoscale allows for the silicon to accommodate the large strain without fracture [5-10]. Nonetheless, the electrochemical performance is still limited due to the uncontrolled solid-electrolyte interphase (SEI) on the surface. Organic electrolyte decomposes at low potential of the anode and forms a thin SEI layer [3, 4]. Due to the repetitive volume expansion and contraction of Si, the SEI layer deforms and breaks. New SEI forms on the fresh exposed silicon,which induces low Coulombic efficiency and consumption of the active material, with the gradually increased SEI eventually blocking Li transport. To solve the above drawbacks, Si/C composites with structure engineering including Si-C yolk structure, pomegranate structure and carbon-coated porous silicon have shown promising results [3, 11-18]. However, the capacity still degraded seriously during the first several cycles due to the inherently weak contact between Si and carbon, which hampers its practical application. Interfacial tailored oxygen and amorphous SiO_2 with a optimized thickness can stabilize the first several cycling performance to a certain extend due to the improved adhesion between Si and carbon [19, 20]. To build a stable SEI layer, a more compact electrolyte blocking layer bonding with Si and an internal void space need to be designed.

In this sense, we present for the first time that the interfacial Si-N-C layer surrounded by mesoporous silicon particles (MSP) enhances the adhesion between Si and C and serves as electrolyte blocking layer, which helps to build a stable SEI layer. Meanwhile, based on micron-sized MSP, we propose a new strategy where the structural stability of the electrode can be dramatically improved by in-situ forming Si nanocrystals at downsizing 5 nm, which is differentiated from the existing methods that focus on controlling the morphology of the nanostructure to withstand the lithiation/delthitation induced enormous mechanical stress. The low Li^+ diffusion kinetics of Si-N-C layer and self limiting inhomogeneous lithiation in MSP jointly creates unlithiated Si nanosrystals, acting as supporting frame to prevent pulverization of the anode material. On the other hand, the nanocrystalline Si particles could enable a fast reversible electrochemical reaction. As a result, the mechanical integrity drastically enhanced, the micro-sized particle still hold together with Si nanocrystals embedded in the amorphous silicon

support frame and no fracture was observed even after 2000 cycles. Thus, the electrodes exhibited an extremely stable electrochemical performance.

Figure 1a schematically illustrates the controllable synthesis of carbon-coated MSP with controllable Si-N-C interlayer by a simple and effective process. The mesoporous silicon film (MSF) with a pore diameter of ~ 20 nm surrounded by uniform walls (~ 10 nm) was synthesized using an electrochemical etching method. With the polyacrylonitrile (PAN) solution as carbon and nitrogen sources, our nitride engineering was enabled with a simple in-situ carbonization method in H_2 and Ar. We proved that the suppression of dehydrogernation process to extent by annealing in H_2 and Ar, which is favor to hold -NH bands. Meanwhile, the surface SiO_x outer MSP was reduced by heat treatment in H_2+Ar. As a result, the surface dangling bonds of fresh amorphous silicon reacted with the surrounded -NH bands to form covalent Si-N bonding. A controllable degree of Si-N-C was synthesized by simply tuning the annealing time.

2 Experimental

2.1 Synthesis of freestanding mesoporous silicon films. MSF was produced by electrochemical etching of heavily boron doped, (100) oriented wafers with a resistivity of 5-7 $m\Omega$ cm by applied a constant current density of 200 mA cm^{-2} for 300s in aqueous 39% hydrofluoric acid (HF)/ethanol electrolyte (HF: EtOH = 5: 1, v-v). To lift off the film, a constant current density of 8 mA cm^{-2} applied for 720s in aqueous 39% hydrofluoric acid (HF)/ethanol electrolyte (HF: EtOH = 1: 10, v: v). The electrochemical etching teflon cell contains a copper plate which connected to a constant-current source, a platinum wire counter electrode and a rubber ring with a diameter of 1.2 cm determines the region to be etched. The distance between the electrodes is 2 cm.

2.2 Fabrication of carbon-coated MSP electrodes. The porous silicon film was mixed with a liquid PAN solution (10 wt. % dissolved in DMF) and ball milled for 1.5 h at 350 r min^{-1}. The recipe contained 20 mg MSP and 200 mg of the above liquid PAN solution. Then, the mixed slurry was spread onto copper foil with a diameter of 14 mm for a current collector and dried for 3 h in a vacuum drying oven at 80 ℃. The obtained PAN coated PSP electrodes were heated in a tube furnace with flowing Ar/H_2 (95% Ar and 5% H_2) at a rate of 5 ℃ min^{-1} to 700 ℃ and held for 1h, 3h and 8h, then naturally cooled to room temperature. The active material loaded on per electrode

is ~ 1 mg.

2.3 Characterization: The morphologies were tested by scanning electron microscopy (SEM) (ZEISS) and transmission electron microscopy (TEM) (Philips Tecnai F30). FTIR X-ray diffraction (XRD) patterns of the samples were obtained by a Rigaku Ultima IV with Cu Ka radiation. X-ray photoelectron spectroscopy (XPS) spectra were acquired with PHI QUANTUM 2000 spectrometer. The nitrogen adsorption and desorption isotherm were tested at 77 K in a range of relative pressure of 0.0001-0.99 P/P_0 using a TriStar II surface area and porosity system (Micromeritics). The active mass was carefully weighted by a microbalance (METTLER TOLEDO XS3DU) with an accuracy of 1 μg.

2.4 Electrochemistry: For electrochemical characterization, the carbon-coated MSP electrodes were assembled into CR2025 coin cells as the working electrodes, with lithium foil being used as the counter electrodes. The electrolyte for all tests was 1M $LiPF_6$ + 10 wt% FEC in ethylene carbonate (EC), and dimethylcarbonate (DMC) (1:1:1 by volume). The galvanostatic cycling of the assembled cells was tested on a Land CT2001A system between 0.005 V and 2.5 V at the temperature of 30 ℃.

3 Results and discussion

Porous silicon film with various pore size prepared by anodic electrochemical etching of single crystalline silicon wafer have been found for more than half a century [21, 22]. In this paper, a heavily boron doped silicon wafer (5-7 $m\Omega \cdot cm$) was used to fabricate MSF (Figure 1b and 1c). At a low magnification side view (Figure 1b), the MSF with a thickness up to ~50 um owning the appearance of small condense pinhole structure. The porous structure with a pore diameter of ~20 nm surrounded by walls (~ 10 nm) was observed at a high magnification top view (Figure 1c). Figure 1d shows the TEM image of MSP, the pores are of ~20 nm in diameter surrounded by thin walls of ~8 nm, inconsistent with the SEM results. High-solution TEM (HRTEM) images (Figure 1e and 1f) show that the MSP wall consists of a polycrystalline Si skeleton coated with a thin amorphous silicon oxide layer of 1-2 nm in thickness, confirming by the energy dispersive X-ray (EDX) spectroscopy line-scanning analysis (Figure 1g). The line signal of Si shows a periodic distribution of 30 nm, which was consistent with the above results. Nitrogen gas adsorption (Figure S1) was also tested and the surface area is 189.9 m^2 g^{-1} calculated by the

Brunauer-Emmett-Teller theory.

After surface nitride process, the MSP with a size of ~2 um dispersed uniformly in the carbon network (Figure 1h and 1i), the carbon framework could serve as mechanical support and provide fast electron pathway. A well pore structure was still held after heat treatment and a carbon layer was outer the MSP with a nonfilling configuration (Figure 1j).To investigate the silicon oxide content of carbon-coated MSP annealed in Ar+H_2 with an increased time, we carried out the HRTEM images of those samples (Figure 2a-2c). The silicon oxide layers outline was hard to observe when annealed for 1h and amorphous material was observed in those areas. Increased the annealing time to 3h, the silicon oxide layers in the skeleton of MSP disappeared and the silicon nanocrystals were embedded in an amorphous network (Figure 2b). Considering that the inner silicon pores of MSP were not coated by carbon layer, we conclude that the silicon oxide layer was reduced by H_2 and the amorphous layer may be amorphous silicon. The MSP skeleton exhibited bigger silicon nanocrystals when annealed for 8h (Figure 2c) due to the surface silicon oxide was reduced. Figure S2 shows the edges views of the above composites, which exhibit a same oxygen variation trend with increased annealing time. Simple by heat treatment of PAN-coated MSP in Ar+H_2 for a certain time, the surface silicon oxide layer was reduced to fresh amorphous silicon with dangling bands.

To reveal the pyrolysis process of PAN in Ar+H_2 and to elucidate the role of H_2, we carried out the Fourier transform infrared (FTIR) spectra of PAN powders and changes of characteristic IR bands with increasing annealing temperature in Ar+H_2 (Figure 2d). In the spectrum collected for the PAN powders, the peaks at 2937 cm^{-1} and 2871 cm^{-1} are assigned to the aliphatic stretching of CH_2 and CH groups in the hydrocarbon chain polymer backbone, respectively [23, 24]. Furthermore, the bands at 1452 cm^{-1} and 1359 cm^{-1} are ascribed to bending of CH and CH_2 groups. The sharp peak at 2245 cm^{-1} is due to the stretching of -CN triple bonding in the nitrile group side chain [23, 24]. It should be noticed that the bands at 1072 cm^{-1} (C-O-C stretch) and 1630 cm^{-1} (C=N stretch) may due to the oxidation and pyrolysis of PAN during the drying process in the sample preparation. The treatment at raised temperature (300 ℃-400 ℃) in Ar+H_2 has apparently decreased nitrile peak (2245 cm^{-1}), CH_2 stretching band (2937 cm^{-1}) and CH_2 bending band (1452 cm^{-1}) in intensity while the peak intensity of −CH bending (shifting to1380 cm^{-1}) has increased at 300 ℃. New IR peaks have appeared at 1605 cm^{-1}, 1270 cm^{-1}, and 1150 cm^{-1}, which are ascribed

to C=C and/or C=N or C-N groups. Moreover, the N-H band at 3410 cm^{-1} has been attributed to the initiation stage of cyclization [23, 25, 26]. The above information suggests that nitrile group of PAN is polymerized to a conjunct CN polymer parallel and dehydrogen process of PAN. However, the retention peak of the CH_2 stretching band (2937 cm^{-1}) indicates that C=C groups are not formed to a significant extent at 300 ℃-400 ℃. Increasing the temperature to 500 ℃, nitrile peak (2245 cm^{-1}) and CH_2 stretching band (2937 cm^{-1}) disappear. The IR peaks at 1380 cm^{-1}, 1270 cm^{-1}, and 1150 cm^{-1} decreased but still a strong adsorption at 1605 cm^{-1}, meaning the existence of conjunct C=C and/or C=N or C-N groups. When the temperature was up to 700 ℃, two broad peaks between 1000 cm^{-1}-1650 cm^{-1} were observed. But the N-H band at 3410 cm^{-1} still existed, implying the suppression of dehydrogenation compared to the thermal treatment of PAN in an inert gas [23, 25]. On the other hand, the surface silicon oxide layer was reduced to fresh amorphous silicon with dangling bands. It could be expected that controlled Si-N-C interlayer may form by annealing in Ar+H_2 for a certain time (Figure S3).

To quantify the interfacial bonding of Si, C and N and to reveal the reaction mechanism of PAN-coated MSP annealed in Ar+H_2, X-ray photoelectron spectroscopy (XPS) and the fitting results (Figure S4) were carried out. The C1s spectrum for the PAN-coated MSP (Figure 2e) includes two components with chemical shifts corresponding to: CH_2 groups (285.4 eV) and C-N triple bonding (286.4 eV). As expected, a single peak at 389.8 eV of the N1s spectrum was observed, indicating the C-N triple bonding in the PAN chains [27-30]. Even annealed in Ar+H_2 for 1h, the main peak of C1s spectrum still located at 285.4 eV, suggesting a certain amount of CH_2 groups in the composites and further confirming the dehydrogenation process of PAN is suppressed in Ar+H_2. In addition, small new peaks at 284.8 eV, 285.8 eV and 287.5 eV obtained by peak fitting suggests that the bonding forming of graphitic sp^2 carbon atoms, doped nitrogen atoms to be sp^2-C and sp^3-C atoms, respectively [31, 32]. Due to the disordering of the graphite-like structure after introduction of nitrogen, the peak of graphitic sp^2 carbon atoms located at a higher binding energy of 284.8 eV [32]. However, increasing the annealing time to 3h results in a main strong peak at 284.8 eV at of C1s high-resolution spectra, indicating forming a large amount of N-doping graphitic sp^2 carbon atoms. Similarly, 285.8 eV and 287.5 eV obtained by peak fitting suggests that the bonding forming of graphitic sp^2 carbon atoms, doped nitrogen atoms to be sp^2-C and sp^3-C atoms, respectively. Even the annealing time up to 8h, the main peak

of N-doping graphitic sp^2 carbon atoms still located at 284.8 eV, however, the peak of doped nitrogen atoms sp^2-C decreased (285.8 eV) and the peak intensity of doped nitrogen sp^3-C atoms (287.5 eV) increased, suggesting the increasing content of N-doped sp^3-C atoms. The N1s scan of PAN-coated MSP (Figure 2f) shows a strong peak at 389.8 eV (C-N triple bonding), resulting from the suppression of dehydrogenation causes a suppression of denitrification. The other two fitting peaks at 400.7 eV and 401.7 eV, which are assigned to pyrrolic N and graphitic N, respectively, indicating that the existence of N-doped amorphous carbon [29-32]. The N1s high-resolution spectrum shows consistent results, the peak is comprised of three components: pyridinic N (398.3 eV), pyrrolic N (400.3 eV) and graphitic N (401.7 eV). Among these three styles of N binding, the pyridinic N is the most favorable for facilitating the electronic conductivity of the carbon layer and the charge transfer at the interface in Li-ion batteries. The graphitic N (401.7 eV) increased and the ratio of pyrrolic N to pyridinic N decreased from 1.3 to 0.7. The Si 2p scan (Figure 2g) indicates that a large amount of silicon oxide (103.3 eV) on the surface of MSP (99.3 eV), inconsistent with the TEM results (Figure 1f).Then annealed in Ar+H2 for 1h, the relative peak intensity of Si grown weak, indicating a new interlayer forms, however, the strong peak of the SiO_2 (103.3 eV) suggests that the interlayer was not formed to a significant extent. Nonetheless, the Si 2p signal shifted to lower binding energy and the Si (99.3 eV) signal disappeared when annealed for 3h, revealing the formation of Si-N (101.8 eV) to an extent. When annealed for 8h, the Si signal exhibits a clear peak at 101.8 eV, however, the interlayer Si-N-C is stable due to it owns a similar peak shape with that of carbon-coated MSP annealed for 3h. The XRD patterns of carbon-coated MSP after annealing are shown in Figure S5. Both the patterns show broad peak around 25^o corresponding to amorphous carbon. The series peaks at 28.4^o, 47.3^o and 56.1^o demonstrate the cubic crystalline nature of Si. However, the relative diffraction intensity of Si was lower when annealed for 8h, which may due to the improved graphitic degree of carbon layer. However, no diffraction peaks of crystalline SiN_x were observed, implying its amorphous nature. As a result, we have synthesized carbon-coated MSP with controlled amorphous Si-N-C interfacial layer, which further confirming the reaction mechanism illustrated in Figure S3.

To provide further evidence for cyclized-PAN's delocalized sp^2 π bonding directly, we use Raman spectroscopy (Figure S6). Both the D (1355 cm^{-1}) and G (1482 cm^{-1}) bands were observed, the two bands are assigned to delocalized sp^2 π bonding, which attributing to the disordered and

ordered structural configurations, respectively [33, 34]. The degree of order was calculated by the integrated ratio of the D and G bands (I_D/I_G). The ratios of carbon-coated MSP annealed in Ar+H_2 for 1h, 3h and 8h were 2.11, 2.12 and 1.67, suggesting PAN continues to pyrolysis from 1h to 3h. However, the I_D/I_G ratio decreased when annealing carbon-coated MSP in Ar+H_2 for 8h, indicating a higher degree of order, inconsistent with the XPS results. Like graphite, pyridine-rings have delocalized sp^2 π bonding which enables good electronic conductivity [35, 36].

The electrochemical properties of carbon-coated MSP electrodes are shown in Figure 3. The gravimetric capacity was calculated based on the mass of entire electrode, considering the SiO_2 and amorphous C may contribute to the total capacity [37-39]. After annealing, the elemental contents of C, N, H, Si is shown in supporting information as table 1. To evaluate the effect of H_2 on the reduction of surface silicon oxide, we heated PAN-coated MSP electrodes with flowing Ar environment at a rate of 5 ℃ min^{-1} to 700 ℃ and held for 1h, then naturally cooled to room temperature. The TEM image of carbon-coated MSP electrode annealed in Ar for 1h is shown in Fig.1a, a SiO_x layer with a thickness of ~2 nm was clearly observed on the surface of MSP. However, when annealed in Ar+H_2 for 1h, the surface silicon oxide was hard to see (Fig. 1b). Based on the above information, compared to the reduction of bulk silica, we conclude that nanoscale surface silicon oxide on MSP was reduced by annealing in Ar+H_2 for a long time. For carbon-coated MSP annealed in Ar+H_2 for 1h, an initial reversible capacity of 1066 mAh g^{-1} with a 70.2% efficiency was achieved at 0.2 A g^{-1}. After the first three cycles, the capacity appeared an approximate linear attenuation of 1.735 mAh g^{-1} per cycle. After 200 cycles, a capacity of 719 mAh g^{-1} was achieved, 67% capacity retention of the first cycle. Increased the annealing time Ar+H_2 to 3h, the electrode exhibited an initial delithiation capacity of 1122 mAh g^{-1} but decreased rapidly to 877 mAh g^{-1} for the first 20 cycles, followed by a linear attenuation to 606 mAh g^{-1} after 200 cycles, only a 54% capacity retention of the first cycle. Considering the electrode of carbon-coated MSP annealed in Ar+H_2 for 3h showed a lower the coulombic efficiency (~97.9%) than that of carbon-coated MSP annealed in Ar+H_2 for 1h and ~98.4%. We believe that the serious capacity decay of carbon-coated MSP annealed in Ar+H_2 for 1h and 3h is due to the relatively unstable SEI layer, because the native silicon oxide can also store Li^+, forming a stable $Li_2Si_2O_5$ and helps to construct a stable SEI layer [20, 39]. The above information further confirms that a certain amount of nanoscale surface silicon oxide on MSP was reduced by annealing in Ar+H_2. To

investigate the long life cycle performance, galvanostatic cycling performance of carbon-coated MSP annealed in Ar+H_2 for 1h and 3h at 1 A g^{-1} were tested (Figure S8). Both electrodes faded seriously during first 20 cycles due to the unstable SEI layer. The capacity retention of carbon-coated MSP annealed in Ar+H_2 for 1h was 30% or 283 mAh g^{-1} after 440 cycles. A 24% capacity retention or 236 mAh g^{-1} was achieved of carbon-coated MSP annealed in Ar+H_2 for 3h after 400 cycles.

The carbon-coated MSP with thick Si-N-C interlayer (annealed in Ar+H_2 for 8h) significantly improved the electrochemical cycling stability. The overpotential is determined by the proportion of Si-N-C with low Li diffusivity [40] at the surface of MSP and this sluggish diffusion kinetics of Li into Si increases the mass transfer resistance, thus resulting in the increase of the overpotential that is required "extra voltage" to drive a Faraday current. As shown in Figure 3d, the polarization potential of carbon-coated MSP cell annealed in Ar+H_2 for 1h is bigger than that of carbon-coated MSP annealed for 3h. Nonetheless checking the lithiation voltage profile of carbon-coated MSP, a short plateau at 0.25 V assigned to a-Si [41] was observed, which further confirmed the reduction effect of H_2 on silicon oxide. As expected, the polarization potential of carbon-coated MSP cell annealed for 8h was significantly increased. For example, the polarization potentials at a half reversible capacity were 0.42 V (annealed in Ar+H_2 for 1h), 0.36 V (annealed in Ar+H_2 for 3h) and 0.54 V (annealed in Ar+H_2 for 8h), respectively. As a result, less active material (inner MSP) interact with Li^+ heterogeneously and a relative low initial reversible capacity of 524 mAh g^{-1} was delivered at 0.1 A g^{-1}. However, for the first time, such a carbon-coated MSP anode was deeply cycled at 0.1 A g^{-1} for 400 cycles under a long life test of more than 6 months, retaining 540 mAh g^{-1} or 100% of its first reversible capacity. The success of excellent long life stable cycling performance was mainly attributed to the inner void space of the mesoporous silicon sponge and the compact interfacial Si-N-C with low Li^+ diffusion kinetics, which enhances the structure integrity and serves as electrolyte blocking layer, respectively.

To optimize the thickness of interfacial Si-N-C layer and to reduce the mass transfer resistance of carbon-coated MSP with favorable stable cycling performance, carbon-coated MSP annealed in Ar+H_2 for 4h, 6h were carried out (Figure 3e). Clearly, the rate performance of carbon-coated MSP annealed in Ar+H_2 was significantly improved by decreasing the annealing time. For example, the capacity retention of carbon-coated MSP annealed in Ar+H_2 for 8h at 2 A g^{-1} was 20%

of that at 0.1 A g^{-1}. However, the capacity retentions of carbon-coated MSP annealed in Ar+H_2 for 6h and 4h are 34% and 42%, respectively. After the rate performance test, the coin cell containing carbon-coated MSP annealed in Ar+H_2 for 6h was cycled for additional 1950 cycles at 0.5 A g^{-1}, maintaining 394 mAh g^{-1} or 100% of its reversible capacity (383 mA h g^{-1}), which further confirms the excellent cyclic performance of carbon-coated MSP anodes. The coulombic efficiency is >99.9 % due to the accuracy limitation of test equipments. To our best knowledge, the carbon-coated MSP anode has marked for the first time that 100% capacity retention was obtained at 0.5 A g^{-1} after 2000 cycle (1950 cycles at 0.5 A g^{-1} following by 10 cycles each at 0.1, 0.5, 1, 2 and 1 A g^{-1}). For example, Liu et al. [3] synthesized silicon pomegranates that can retain 97% of their initial capacity after 1000 cycles at a constant-charge rate. Li et al. [13] prepared pre-lithiated mesporous silicon sponge (MSS) anodes, which can deliver a capacity of ~640 mA h g^{-1} with 81% capacity retention over 1000 cycles. However, the capacity retention is ~ 82% after 800 cycles (10 cycles each at 0.1, 0.25, 0.5, 1, 2, and 4 A g^{-1} and then 740 cycles at 1 A g^{-1}). Wang et al. [42] controllably synthesized graphene sheet-supported uniform ultra-small (~3 nm) silicon quantum dots anodes, the charge capacity retention was 98% after 500 cycles.

To further reveal the significant role of interfacial Si-N-C to electrochemical cycling stability, electrodes containing carbon-coated MSP were opened and soaked in DMC for more than 24h to remove the residual electrolyte. XPS spectrum of carbon-coated MSP annealed in Ar+H_2 for 3h and 8h after 200 cycles were obtained (Figure S9). Clearly, a relatively strong peak at 397.5 eV (Si-N bonding) was observed of carbon-coated MSP annealed in Ar+H_2 for 8h, implying a stable Si-N-C interfacial layer during cycling. Checking the surface structure, no fracture of the separate particles was observed even after a long life cycle (Figure S10), implying the SEI layer was not too thick. TEM images of cycling carbon-coated MSP are shown in Figure 4, silicon crystals with a size of ~ 3 nm (Figure 4b) or ~8nm (Figure 4e) were observed. The sizes differences were caused by the charge/discharge current density. A lower current induces more homogeneous and more thoroughly alloy/dealloy reaction. The silicon nanocrystals mainly caused by the two factors: (1) the sluggish diffusion of Li^+ in the Si-N-C layer hinders the inner silicon interact with Li^+. Though the pores inner MSP was almost filled, the MSP particles still not fully lithiated due to the remaining silicon nanocrystalline particles; (2) the self-limiting lithiation in MSP during repeated cycles, which is attributed the retardation effect of lithiation stress [10, 43]. The amorphous Li_xSi

grows around the during the lithiation process. The remaining silicon nanocrystalline particles act as supporting frame to prevent pulverization of the anode material. On the other hand, the nano-Si silicon nanocrystals could enable a fast reversible electrochemical reaction. As a result, the mechanical stability of MSP during cycling improves progressively.

In summary, simple by a controlled thermal treatment in $Ar+H_2$, the dehydrogernation process of PAN was depressed and the surface silicon oxide outer MSP was reduced. Consequently, the remaining -NH bands of carbon chain can interact with the surface fresh amorphous Si to form Si-N-C layer. The thickness of Si-N-C layer was optimized by varying the annealing time. Our nitrogen engineering MSP anode has marked for the first time that a 100% capacity retention (394 mA h g^{-1}) after 2000 cycle (10 cycles each at 0.1, 0.5, 1, 2, and 1 and then 1950 cycles at 0.5 A g^{-1}) and a 100% capacity retention at 0.1 A g^{-1} (540 mA h g^{-1}) after 400 cycles. We attribute superior stable battery performance to the stable interfacial Si-N-C electrolyte blocking layer and the remaining unlithiated nano-Si seeds acting as support frame to prevent pulverization of composite material. Thus, our work proposes a novel avenue to engineer battery materials with large volume changes.

Supporting Information

Supporting Information is available from the RSC publication or from the author.

Acknowledgements

The authors gratefully acknowledge the support of the National Natural Science Foundation of China under grant nos. 61474081, 61534005 and 21233004.

References

1. C. K. Chan, H. Peng, G. Liu, K. Mcilwrath, X. F. Zhang, R. A. Huggins, Y. Cui, *Nat. Nanotech.*, 2008, **3**, 31-35.
2. R. Yi, F. Dai, M. L. Gordin, S. Chen, D. Wang, *Adv. Energy Mater.*, 2013, **3**, 295-300.
3. N. Liu, Z. Lu, J.Zhao, M. T. McDowell, H. W. Lee, W. Zhao, Y. Cui, *Nat. Nanotech.*, 2014, **9**, 187-192.
4. X. K. Huang, J. Yang, S. Mao, J. Chang, P. B. Hallac, C. R. Fell, J. Chen, *Adv. Mater.*,2014, **26**, 4326-4332.
5. A. Magasinski, P. Dixon, B. Hertzberg, A. Kvit, J. Ayala, G. Yushin, *Nat. Mater.*, 2010, **9**,

353-358.
6. H. Tang, J. P. Tu, X. Y. Liu, Y. J. Zhang, S. Huang, W. Z. Li, C. D. Gu, *J. Mater. Chem. A*, 2014, **2**, 5834-5840.
7. G. Liu, S. Xun, N. Vukmirovic, X. Song, H. Zheng, W. Yang, *Adv. Mater*., 2011, **23**, 4679.
8. H. Wu, Y. Cui, *Nano Today*, **2012**, *7*, 414-429.
9. X. H. Liu, L. Zhong, S. Huang, S. X.Mao, T. Zhu, J. Y. Huang, *ACS Nano*., 2012, **6**, 1522-1531.
10. M. T. McDowell, S. W. Lee, W. D. Nix, Y. Cui, *Adv. Mater.* **2013**, *25*, 4966-4985.
11. B. Wang, T. Qiu, X. Li, B. Luo, L. Hao, Y. Zhang, L. Zhi, *J. Mater. Chem. A*, 2014, **3**, 494-498.
12. X. Han, H. X. Chen, J. J. Liu, P. Wang, K. Huang, C. Li, S. Y. Chen, Y. Yang, *Electrochim. Acta*, 2015, **156**, 11-16.
13. X. Li, M. Gu, S. Hu, R. Kennard, P. Yan, X. Chen, J. Liu, *Nat. Commu*., 2014, **5***,* 105.
14. Z. Lu, N. Liu, H. W. Lee, J. Zhao, W. Li, Y. Li, Y. Cui, *ACS Nano*, 2015, **9**, 2540-2547.
15. H. T. Nguyen, M. R. Zamfir, L. D. Duong, Y. H. Lee, P. Bondavalli, D. Pribat, *J. Mater. Chem.*, 2012, **22**, 24618-24626.
16. Y. Fan, Q. Zhang, C. Lu, Q. Xiao, X. Wang, *Nanoscale*, 2013, **5**, 1503-1506.
17. J. Song, S. Chen, M. Zhou, T. Xu, D. Lv, M. L. Gordin, D. Wang, *J. Mater. Chem. A*, 2014, **2**, 1257-1262.
18. F. Dai, J. Zai, R. Yi, M. L. Gordin, H. Sohn, S. Chen, D. Wang, *Nat. Commu*., 2014, **5**, 3605.
19. C. F. Sun, H. Zhu, M. Okada, K. J. Gaskell, Y. Inoue, L. Hu, Y. Wang, *Nano Lett*., 2015, **15**, 703-708.
20. S. Sim, P. Oh, S. Park, J. Cho, *Adv. Mat.,* 2013, **25**, 4498-4503.
21. M. J. Sailor, John Wiley & Sons **2012**.
22. H. Föll, M. Christophersen, J. Carstensen, G. Hasse, *Mater. Sci. Eng., R*, 2002, **39**, 93-141.
23. T. C. Chung, Y. Schlesinger, S. Etemad, A. G. Macdiarmid, A. J. Heeger, *J. Polym. Sci. Pt. B-Polym. Phys.*, 1984, **22**, 1239-1246.
24. X. Gi, J. Dong, J. F. Zhang, *Macromolecules*, 1992, **25**, 5855-5857.
25. J. E. Bailey, A. J. Clarke, *Nature*, 1971, **234**, 529-531.
26. C. Songyan, P. K. Kashkarov, V. Y. Timoshenko, L. Baolin, J. Bingxi, *J. Cryst. Growth*, 2003, **247***,* 445-451.
27. R. Janus, P. Natkański, A. Wach, M. Drozdek, Z. Piwowarska, P. Cool, P. Kuśtrowski, *J. Therm. Anal. Calorim*., 2012, **110**, 119-125.
28. D. M. Piper, T. A. Yersak, S. B. Son, S. C. Kim, C. S. Kang, K. H. Oh, S. H. Lee, *Adv. Energy Mater.*, 2013, **3**, 697-702.
29. H. Mi, Y. Li, P. Zhu, X. Chai, L. Sun, H. Zhuo, J. Liu, *J. Mater. Chem. A*, 2014, **2**, 11254-11260.
30. L. Shen, Z. Wang, L. Chen, *ChemSusChem*, 2014, **7**, 1951-1956.
31. Z. H. Sheng, L. Shao, J. J. Chen, W. J. Bao, F. B. Wang, X. H. Xia, *Acs Nano*, 2011, **5**, 4350-4358.
32. J. Wu, X. Qin, H. Zhang, Y. B. He, B. Li, L. Ke, F. Kang, *Carbon*, 2015, **84**, 434-443.
33. A. C. Ferrari, J. Robertson , *Philos.Trans. Royal Soc. A*, 2004, **362**, 2477-2512.
34. C. Kim, S. H. Park, J.I. Cho, D.Y. Lee, T. J. Park, W. J. Lee, K. S. Yang, *J. Raman Spectrosc.*, 2004, 35, 928-933.

35. W. X. Zhang, Y. Z. Wang, C.F. Sun, *J. Polym. Res.*, 2007, **14**, 467-474.
36. A. Ferrari, J. Robertson, *Phys. Rev. B,* 2001, **64**, 1-13.
37. J. R. Dahn, T. Zheng, Y. H. Liu, J.S. Xue, *Science*, 1995, **270**, 590-593.
38. J. Yang, R. C. de Guzman, S. O. Salley, K. S. Ng, B. H. Chen, M. C. Cheng, *J. Power Sources*, 2014, **269**, 520-525.
39. M. T. McDowell, S. W. Lee, I. Ryu, H. Wu, W. D. Nix, J. W. Choi, Y. Cui, *Nano Lett*., 2011, **11**, 4018-4025.
40. Z. Wen, K. Wang, L. Chen, J. Xie, *Electrochem. Commun*., 2006, **8**, 1349-1352.
41. L. F. Cui, R. Ruffo, C. K. Chan, H. Peng, Y. Cui, *Nano Lett*., 2008, **9**, 491-495.
42. B. Wang, X. Li, B. Luo, L. Hao, M. Zhou, X. Zhang, L. Zhi, *Adv. Mater.*, 2015, **27**, 1526-1532.
43. X. H. Liu, F. Fan, H. Yang, S. Zhang, J. Y. Huang, T. Zhu, *Acs Nano*, 2013, **7**, 1495-1503.

Figure Captions

Figure 1. (a) Schematic inllustrtion of fabricting Si@Si-N-C@C MSP. (b) Side-view SEM image of MSF. (c) Top-view SEM image of MSF. d) TEM image of MSP. (e) High resolution TEM (HRTEM) image of the pores in MSP. (f) HRTEM image of MSP edge, inset is FFT parttern of the area in Figure 1f. (g) Dark-field TEM image of MSP and corresponding EDX elemental line-scanning of Si and O. (h) SEM image of carbon-coatd MSP particles. (i) TEM image of MSP particles embedded in carbon framework. (j) TEM image of individual carbon-coated MSP particle.

Figure 2. HRTEM images of carbon-coated MSP annealed in $Ar+H_2$ for 1h (a), 3h (b) and 8h (c). (d) FTIR spectra of PAN powders and changes of characteristic IR bands with increasing annealing temperature in $Ar+H_2$. (e)-(g) X-ray photoelectron spectroscopy (XPS) spectrum of PAN-coated MSP (black), annealed in $Ar+H_2$ for 1h (red), 3h (blue) and 8h (green).

Figure 3. (a) Galvanostatic cycling performance of carbon-coated MSP annealed in $Ar+H_2$ for 1h (red) and 3h (blue). (b) Rate performance of carbon-coated MSP annealed in $Ar+H_2$ for 1h (red) and 3h (blue). (c) Galvanostatic cycling performance of carbon-coated MSP annealed in $Ar+H_2$ for 1h at 0.1 A g^{-1}. (d) Initial charge-discharge profiles at a charge/discharge rate of 0.1 A g^{-1} of carbon-coated MSP annealed in $Ar+ H_2$ for 8h (blue), and 0.2 A g^{-1} of carbon-coated MSP annealed in $Ar+ H_2$ for 1h (black) and 3h (red). (e) Long life cycling performance at 0.5 A g^{-1} after rate testing of carbon-coated MSP annealed in $Ar+H_2$ for 4h (blue), 6h (black) and 8h (red).

Figure 4. (a)-(c) TEM images of carbon-coated MSP annealed in $Ar+H_2$ for 8h after 200 cycles at 0.1 A g^{-1}. (d)-(e) TEM images of carbon-coated MSP annealed in $Ar+H_2$ for 4h after 2000 cycles at 0.1 A g^{-1}. (f) FFT pattern of the TEM image in (e).

Figure 1.

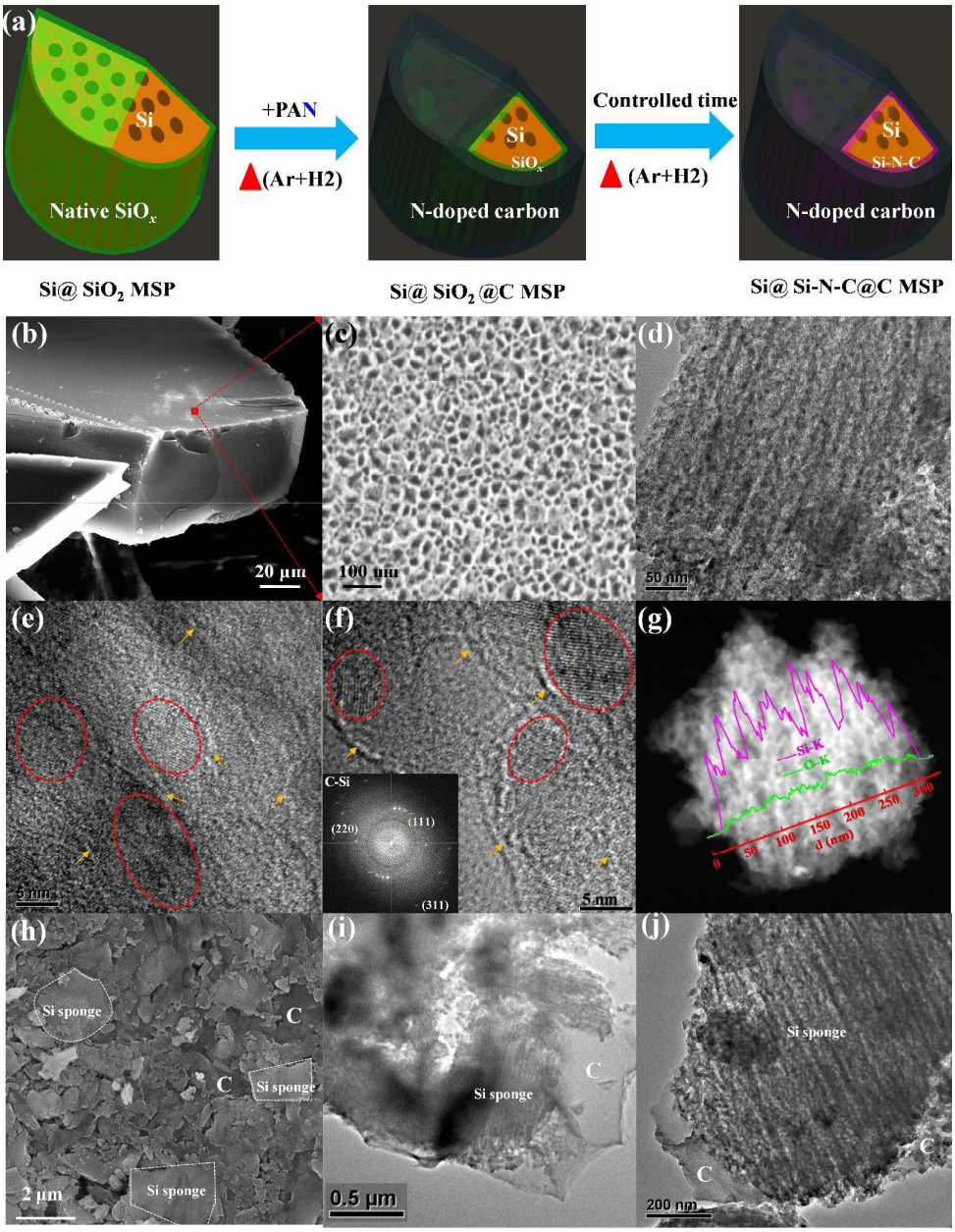

Figure 2.

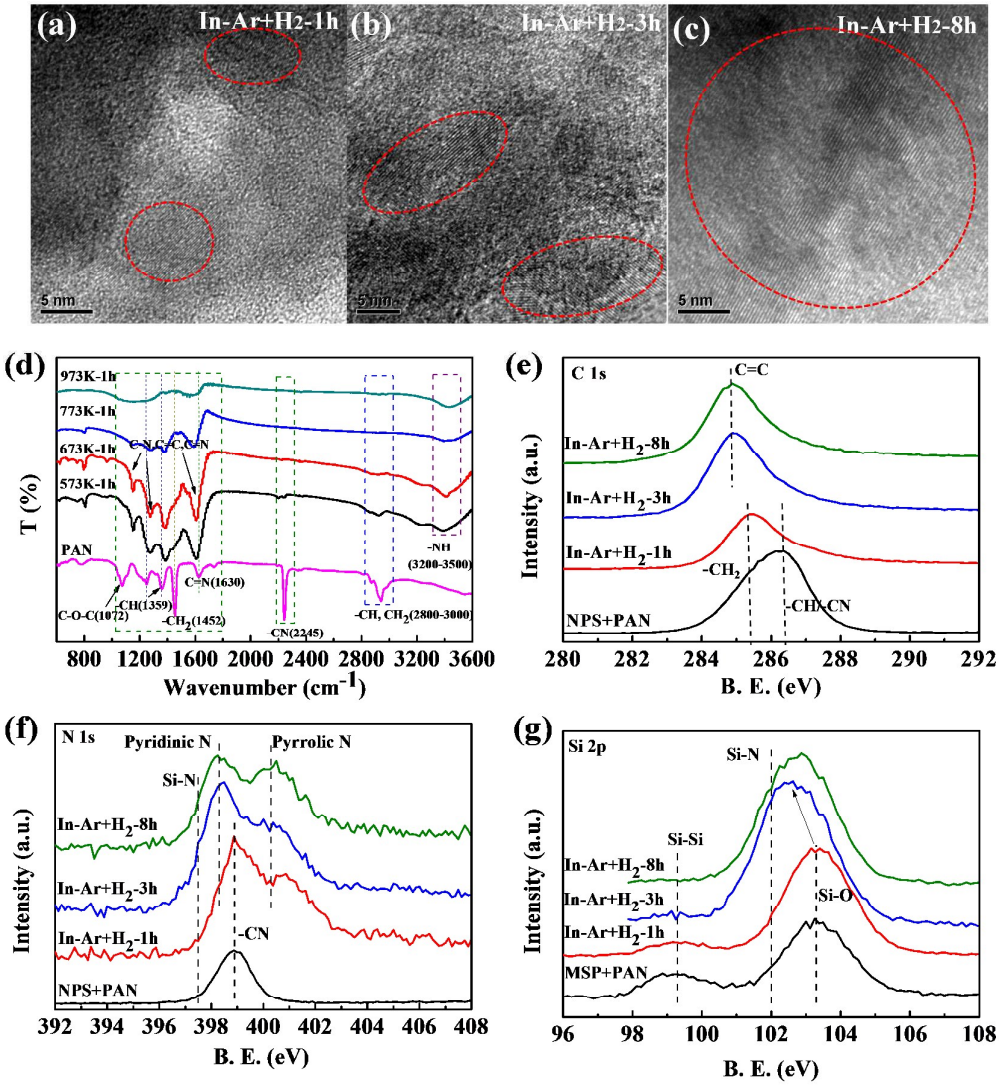

Figure 3.

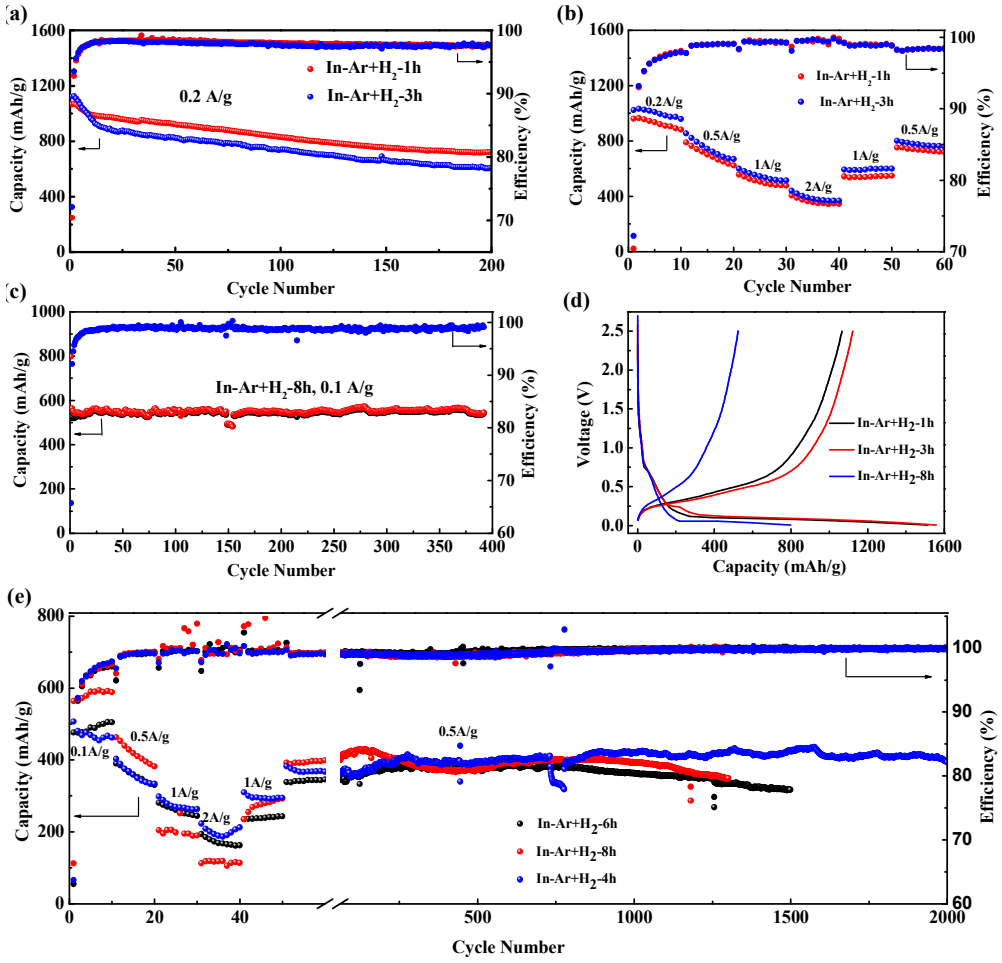

Figure 4.

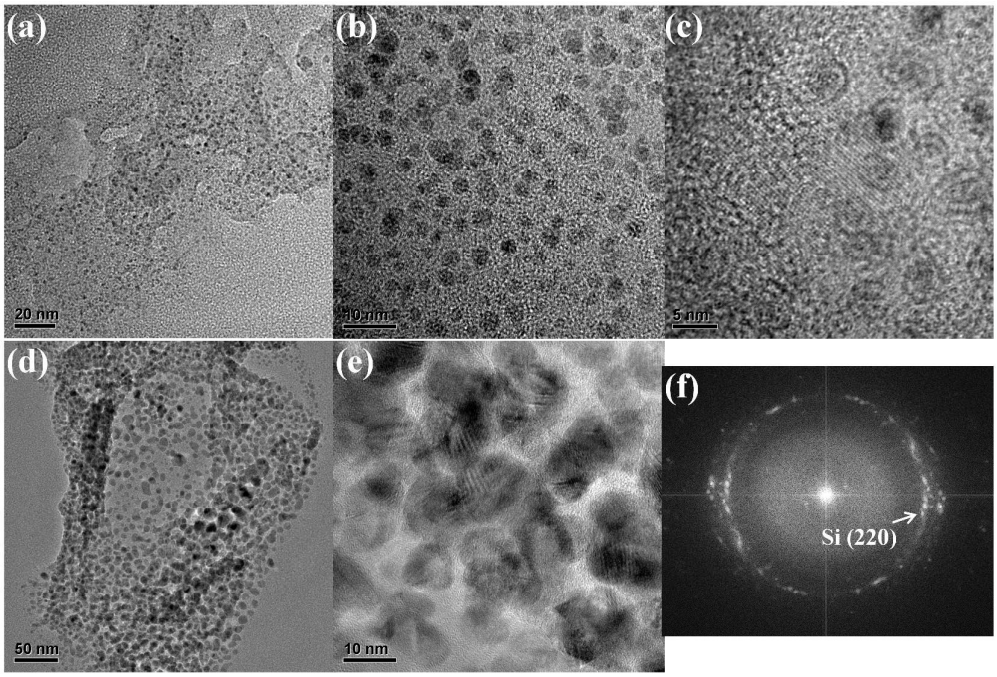

Table of contents